Original
Received January 10, 2006
Accepted for Publication March 10, 2006

Ballistic Limits of Gr/Ep and Hybrid Composite Rear Walls Protected by a Debris Shield

Ryo ITO* and Hideki SEKINE**

*Graduate School of Engineering, Tohoku University,
6-6-01 Aoba-yama, Aoba-ku, Sendai, 980-8579, Japan
**Department of Aerospace Engineering, Tohoku University,
6-6-01 Aoba-yama, Aoba-ku Sendai, 980-8579, Japan
E-mail : sekine@plum.mech.tohoku.ac.jp

Protecting spacecraft against hypervelocity impacts (HVIs) of space debris, which may cause fatal damage to the spacecraft, has attracted much attention. In this study, we conduct the numerical simulation of HVIs of a projectile on rear walls protected by a debris shield. To numerically simulate the HVIs, an improved smoothed particle hydrodynamics (SPH) method with new particle generation and particle merger techniques is used. Through the numerical simulation, we evaluate the total kinetic energy of debris cloud through unit area on the top surface of rear wall, and discuss the ballistic limits of the graphite/epoxy (Gr/Ep) and hybrid composite rear walls. Consequently, we provide the data needed for designing the rear walls.

Key Words : Numerical simulation; SPH method; Hypervelocity impact; Ballistic limit; Spacecraft structure

1 Introduction

The debris shield which is spaced at a given standoff distance from rear walls is a conventional means for providing protection to the rear walls against hypervelocity impacts (HVIs) of space debris. Thus far, the protection capability of debris shields and the perforation resistance of rear walls have been studied experimentally by ground-based HVI tests. However, in those tests the impact velocity and the size of projectiles were limited, and comprehensive understanding of the protection capability of debris shields and the perforation resistance of rear walls has not been obtained. With this situation, numerical simulation could provide a more efficient way to study this problem.

In the numerical simulation of HVIs, a hydrodynamics method is usually adopted to take account of the melting of materials by heat generation, and a smoothed particle hydrodynamics (SPH) method[1,2] is especially attractive. Recently, Hayhurst et al.[3] and Palmieri et al.[4] conducted numerical simulation of HVIs using an SPH method to study the protection capability of debris shields. In those studies, the protection capability was represented by ballistic limit curves of rear wall. However, those curves have not provided the sufficient data for designing debris shields and rear walls.

In this study, our concern is to obtain the data needed for designing rear walls. We conduct the numerical simulation of HVIs of a projectile on rear walls protected by a debris shield. To numerically simulate the HVIs, an improved SPH method with new particle generation and particle merger techniques[5] is used. We evaluate the total kinetic energy of debris cloud through unit area on the top surface of rear wall, and discuss the ballistic limits of the graphite/epoxy (Gr/Ep) and hybrid composite rear walls.

2 Theoretical Fundamentals

2.1 Conservation laws

The expressions of the two-dimensional SPH method for the conservation laws of mass, momentum and energy for the ith particle are written as

$$\frac{d\rho_i}{dt}=\rho_i\sum_j\frac{m_j}{\rho_j}\left(u_i^\beta-u_j^\beta\right)W_{ij,\beta} \tag{1}$$

$$\frac{du_i^\alpha}{dt}=\sum_j m_j\left(\frac{\sigma_i^{\alpha\beta}}{\rho_i^2}+\frac{\sigma_j^{\alpha\beta}}{\rho_j^2}-\delta^{\alpha\beta}\Pi_{ij}\right)W_{ij,\beta} \tag{2}$$

$$\frac{de_i}{dt}=\frac{1}{2}\sum_j m_j\left(u_i^\alpha-u_j^\alpha\right)\left(\frac{\sigma_i^{\alpha\beta}}{\rho_i^2}+\frac{\sigma_j^{\alpha\beta}}{\rho_j^2}-\delta^{\alpha\beta}\Pi_{ij}\right)W_{ij,\beta} \tag{3}$$

where ρ_i is the density, m_i is the mass, u_i^α is the velocity, $\sigma_i^{\alpha\beta}$ is the stress and e_i is the specific internal energy of the ith particle, and $\delta^{\alpha\beta}$ is the Kronecker delta. The B-spline function is used as the kernel function $W_{ij}(=W(x_i^\alpha-x_j^\alpha))$, where x_i^α and x_j^α are the position vectors of the ith and jth particles, and $W_{ij,\beta}(=\partial W_{ij}/\partial x_i^\beta)$ is the derivative of the kernel function. Greek indices range over the values 1 and 2, and the usual summation convention is applied to every repeated Greek index. The artificial viscosity Π_{ij} which is introduced to capture shock waves is given by

$$\Pi_{ij}=\frac{1}{\bar{\rho}_{ij}}\left(-a\mu_{ij}\bar{c}_{ij}+b\mu_{ij}^2\right) \tag{4}$$

where

$$\mu_{ij}=\begin{cases}\dfrac{h\left(u_i^\alpha-u_j^\alpha\right)x_{ij}^\alpha}{x_{ij}^\alpha x_{ij}^\alpha+\zeta h^2} & \text{for } \left(u_i^\alpha-u_j^\alpha\right)x_{ij}^\alpha<0\\ 0 & \text{for } \left(u_i^\alpha-u_j^\alpha\right)x_{ij}^\alpha\geq 0\end{cases} \tag{5}$$

and

$$\bar{\rho}_{ij}=(\rho_i+\rho_j)/2,\ \bar{c}_{ij}=(c_i+c_j)/2,\ x_{ij}^{\alpha}=x_i^{\alpha}-x_j^{\alpha} \tag{6}$$

Here, the parameter h in Eq. (5) is the measure of the width of the kernel function, and c_i in Eq. (6) denotes the sound velocity. In this study, the parameters a, b, and ζ are taken as $a=b=2.5$ and $\zeta=0.1$[2].

2.2 Constitutive equations

2.2.1 *Aluminum*: The stress tensor $\sigma^{\alpha\beta}$ is defined in terms of the deviatoric stress $s^{\alpha\beta}$ and the pressure P, as

$$\sigma^{\alpha\beta}=s^{\alpha\beta}-\delta^{\alpha\beta}P \tag{7}$$

It is noted that the mean stress σ^0 is given by $\sigma^0=-P$. To account for the rotation effect caused by the large deformation of materials, the Jaumann rate $\mathring{s}^{\alpha\beta}$ is used. The elastic deviatoric stress rate $\dot{s}^{\alpha\beta}$ is then given by

$$\begin{aligned}\dot{s}^{\alpha\beta}&=\mathring{s}^{\alpha\beta}+s^{\alpha\gamma}\omega^{\beta\gamma}+s^{\gamma\beta}\omega^{\alpha\gamma}\\&=2G\left(\dot{\varepsilon}^{\alpha\beta}-\frac{1}{3}\delta^{\alpha\beta}\dot{\varepsilon}^{\gamma\gamma}\right)+s^{\alpha\gamma}\omega^{\beta\gamma}+s^{\gamma\beta}\omega^{\alpha\gamma}\end{aligned} \tag{8}$$

where G is the shear modulus, and $\dot{\varepsilon}^{\alpha\beta}$ and $\omega^{\alpha\beta}$ are the strain and rotation rate tensors. The SPH expressions of these tensors for the ith particle are derived as

$$\dot{\varepsilon}_i^{\alpha\beta}=\frac{1}{2}\sum_j\frac{m_j}{\rho_j}\left[\left(u_j^{\alpha}-u_i^{\alpha}\right)W_{ij,\beta}+\left(u_j^{\beta}-u_i^{\beta}\right)W_{ij,\alpha}\right] \tag{9}$$

and

$$\omega_i^{\alpha\beta}=\frac{1}{2}\sum_j\frac{m_j}{\rho_j}\left[\left(u_j^{\alpha}-u_i^{\alpha}\right)W_{ij,\beta}-\left(u_j^{\beta}-u_i^{\beta}\right)W_{ij,\alpha}\right] \tag{10}$$

The elastic deviatoric stress in Eq. (7) can be obtained by integrating Eq. (8) with respect to time. The plastic flow regime is determined by the von Mises criterion after the second deviatoric stress invariant J_2 arrives $\sigma_Y^2/3$, where σ_Y is the yield stress. The deviatoric stress is then brought back to the yield surface, and its estimated value $s_{est}^{\alpha\beta}$ is given by

$$s_{est}^{\alpha\beta}=s^{\alpha\beta}\left(\frac{\sigma_Y^2}{3J_2}\right)^{\frac{1}{2}} \tag{11}$$

2.2.2 *Gr/Ep*: In this study, the strain-rate dependent one-parameter visco-plasticity model[6] is used to obtain the constitutive relationship for composite laminas. The elasto-visco-plastic constitutive equation is written as

$$\begin{Bmatrix}\dot{\varepsilon}^{11}\\\dot{\varepsilon}^{22}\\\dot{\varepsilon}^{33}\\\dot{\varepsilon}^{23}\\\dot{\varepsilon}^{31}\\\dot{\varepsilon}^{12}\end{Bmatrix}=\begin{bmatrix}S_e^{11}&S_e^{12}&S_e^{13}&0&0&0\\S_e^{12}&S_{ep}^{22}&S_{ep}^{23}&S_{ep}^{24}&S_{ep}^{25}&S_{ep}^{26}\\S_e^{13}&S_{ep}^{23}&S_{ep}^{33}&S_{ep}^{34}&S_{ep}^{35}&S_{ep}^{36}\\0&S_{ep}^{24}&S_{ep}^{34}&S_{ep}^{44}&S_{ep}^{45}&S_{ep}^{46}\\0&S_{ep}^{25}&S_{ep}^{35}&S_{ep}^{45}&S_{ep}^{55}&S_{ep}^{56}\\0&S_{ep}^{26}&S_{ep}^{36}&S_{ep}^{46}&S_{ep}^{56}&S_{ep}^{66}\end{bmatrix}\begin{Bmatrix}\dot{\sigma}^{11}\\\dot{\sigma}^{22}\\\dot{\sigma}^{33}\\\dot{\sigma}^{23}\\\dot{\sigma}^{31}\\\dot{\sigma}^{12}\end{Bmatrix} \tag{12}$$

where $\dot{\varepsilon}^{\alpha\beta}$ is total strain rate, $\dot{\sigma}^{\alpha\beta}$ is stress rate, $S_e^{\alpha\beta}$ and $S_{ep}^{\alpha\beta}$ are the elastic and elasto-plastic compliances, respectively. The elasto-plastic compliance $S_{ep}^{\alpha\beta}$ is defined as the sum of the elastic compliance $S_e^{\alpha\beta}$ and the plastic compliance $S_p^{\alpha\beta}$.

2.3 Material strength and fracture criteria

2.3.1 *Aluminum*: At a high strain rate, the yield stress σ_Y is given as a function of effective strain $\bar{\varepsilon}$, effective strain rate $\dot{\bar{\varepsilon}}$ and temperature T. In this study, the Johnson-Cook material strength criterion[7] is employed, in which σ_Y is given by

$$\sigma_Y=\left(\sigma_{Y0}+B\bar{\varepsilon}^n\right)\left(1+C\ln\dot{\bar{\varepsilon}}^*\right)\left[1-\left(T^*\right)^m\right] \tag{13}$$

where σ_{Y0}, B, C, n and m are material parameters determined by experiments. Moreover, $\dot{\bar{\varepsilon}}^*=\dot{\bar{\varepsilon}}/\dot{\bar{\varepsilon}}_0$ is the dimensionless effective strain rate for $\dot{\bar{\varepsilon}}_0=1.0\mathrm{s}^{-1}$, and T^* is the homologous temperature defined by

$$T^*=\frac{T-T_{room}}{T_{melt}-T_{room}} \tag{14}$$

where T_{room} is the room temperature which is taken as $T_{room}=300\,\mathrm{K}$, and T_{melt} is the melting temperature.

In the fracture analysis, the Johnson-Cook fracture criterion[7] which is based on the concept of cumulative damage is used, and it can take account of the loading history that may involve variations in strain rate, temperature and pressure. The damage parameter D is defined by

$$D=\sum\Delta\bar{\varepsilon}/\varepsilon_f \tag{15}$$

where $\Delta\bar{\varepsilon}$ is the increment of effective strain caused by tensile load and ε_f is the effective fracture strain in instantaneous conditions. It is noted that the fracture occurs at $D=1$. The effective fracture strain ε_f is given by

$$\varepsilon_f=\left(D_1+D_2\exp D_3\sigma^*\right)\left(1+D_4\ln\dot{\bar{\varepsilon}}^*\right)\left(1+D_5T^*\right) \tag{16}$$

where σ^* is the dimensionless pressure-strain ratio defined as $\sigma^*=\sigma^0/\bar{\sigma}$ for the effective stress $\bar{\sigma}$, and D_1, D_2, D_3, D_4 and D_5 are material parameters determined by experiments. If the fracture criterion is satisfied, the tensile stress between the particles is reset to zero.

2.3.2 *Gr/Ep*: Under the assumptions of linear elasticity in the fiber direction and transverse isotropy for composite laminas, the one parameter yield function is written as

$$2f\left(\sigma^{\alpha\beta}\right)=\left(\sigma^{22}-\sigma^{33}\right)^2+4\left(\sigma^{23}\right)^2+2a^{66}\left[\left(\sigma^{12}\right)^2+\left(\sigma^{13}\right)^2\right] \tag{17}$$

where a^{66} is the parameter which governs the degree of anisotropy in plasticity and is independent of strain rates. Through Eq. (17), the plastic compliance $S_p^{\alpha\beta}$ is given by

$$S_p^{\phi\psi}=\mu C^{\phi}C^{\psi}\quad(\phi,\psi=1,2,..,6) \tag{18}$$

where

$$\begin{aligned}&C^{\gamma}=\frac{\partial f}{\partial\sigma^{\gamma}}\ ;\quad\mu=\frac{9}{4}\frac{1}{\bar{\sigma}^2}\frac{1}{H_p}\\&C^1=0,\quad C^2=\sigma^{22}-\sigma^{33},\ C^3=\sigma^{33}-\sigma^{22}\\&C^4=4\sigma^{23},\ C^5=2a^{66}\sigma^{13},\quad C^6=2a^{66}\sigma^{12}\end{aligned} \tag{19}$$

The plastic modulus H_p is defined as $H_p=d\bar{\sigma}/d\bar{\varepsilon}_p$ where $\bar{\sigma}$ is the effective stress and $\bar{\varepsilon}_p$ is the effective plastic strain. The plastic modulus H_p is obtained using the total stress model[8] in which the effective plastic strain is assumed to be a function of effective plastic strain rate and effective stress.

With respect to the fracture criteria, the maximum stress criteria are applied. That is, if the stress in the fiber direction exceeds the tensile strength, the fracture occurs, and σ^{11}, σ^{12} and σ^{13} are reset to be zero for their remaining steps except for σ^{11} to be compressive.

Equation of state

We employ the Mie-Grüneisen equation of state, which is given by

$$P(\rho, e)=\left(1-\frac{1}{2}\Gamma\eta\right)P_{\mathrm{H}}(\rho)+\Gamma\rho e \tag{20}$$

where Γ is the Grüneisen constant, $\eta=\rho/\rho_0-1$, ρ_0 is the initial density, and P_{H} is the Hugoniot curve which is written as

$$P_{\mathrm{H}}=\begin{cases} a_1\eta+a_2\eta^2+a_3\eta^3 & \eta>0 \\ a_1\eta & \eta<0 \end{cases} \tag{21}$$

Here the constants a_1, a_2 and a_3 can be expressed in terms of the parameters c_0 and ξ, as follows:

$$\begin{aligned} a_1&=\rho_0 c_0^2 \\ a_2&=a_1\left[1+2(\xi-1)\right] \\ a_3&=a_1\left[2(\xi-1)+3(\xi-1)^2\right] \end{aligned} \tag{22}$$

2.5 Procedure of numerical simulation by means of improved SPH method

In the numerical simulation of HVIs by means of a conventional SPH method, the loss of interactions among particles causes "numerical fractures" when the distance between the particles increases. To prevent "numerical fractures", the authors[5] proposed an improved SPH method with new particle generation and particle merger techniques.

The procedure of numerical simulation by means of the improved SPH method is as follows: First, we set all physical quantities at their initial values, and make the triangular elements used in the new particle generation and particle merger. The remainder of the procedure is outlined below. The following calculations are performed for every particle.

Step 1 The differential equations (1), (2), (3), (8) and (9) are solved by the fourth-order Runge-Kutta method. Then, the magnitude of time step Δt is determined from the Courant-Friedrichs-Lewy (CFL) condition, i.e.,

$$\Delta t=\underset{i}{\mathrm{Min}}\left(\frac{\omega h}{c_i+\bar{u}_i}\right) \tag{23}$$

where $\bar{u}_i$ is the absolute velocity of the ith particle, and ω is the constant parameter.

Step 2 Update time t to $t+\Delta t$.

Step 3 Recalculate the pressure, stress and strain rate.

Step 4 The calculations of material strength and fracture criteria are performed through Eqs. (13) to (19).

Step 5 The criteria of new particle generation and particle merger are checked for every certain number of time steps. If the criteria are checked, go to Step 6. Otherwise, go to Step 1. In this study, the criteria are checked for every 10 time steps.

Step 6 If the criterion of new particle generation is satisfied, we generate new particles by the new particle generation technique. Next, if the criterion of particle merger is satisfied, we merge the particles by the particle merger technique. Then, go to Step 1.

Iterate Steps 1 to 6 until time t reaches user-specified end time t_{end}.

Table 1 Material properties of aluminum.

G (GPa)	σ_{Y0}(MPa)	B (MPa)	C (−)	n (−)	m (−)	T_{melt} (K)	C_p (J/gK)
27.6	265	426	0.015	0.34	1.00	775	0.87
D_1 (−)	D_2 (−)	D_3 (−)	D_4 (−)	D_5 (−)	Γ (−)	ρ_0(g/cm^3)	C_0(km/s)	ξ (−)
0.13	0.13	-1.5	0.011	0.0	2.0	2.785	5.33	1.338

3 Numerical Simulation and Discussion

We simulate the HVIs of a projectile on Gr/Ep and hybrid composite rear walls protected by a debris shield, and discuss the ballistic limits of the rear walls.

3.1 Numerical model

The schematic view of HVI of a projectile on a rear wall protected by a debris shield is presented in Figure 1. The standoff distance is taken as 100 mm. The projectile strikes to the debris shield at the impact angle 0°. The boundary conditions are such that the debris shield and the rear wall are free on the edges.

The schematic view of interface of laminated rear walls is illustrated in Figure 2. The interface model is based on the premise that only positive pressure acts between the particles P_A and P_B which belong to layers A and B, respectively, when the two particles are approaching each other.

3.1.1 ***Projectile and debris shield*** : The projectile and debris shield are of aluminum. Unless otherwise stated, the cross section of the projectile is square and its side length is 2 mm, i. e., the mass per unit length is 0.11 g/cm, and the debris shield is $W_d=30$ mm in width and $H_d=1.4$ mm in thickness. The material properties of aluminum are given in Table 1.

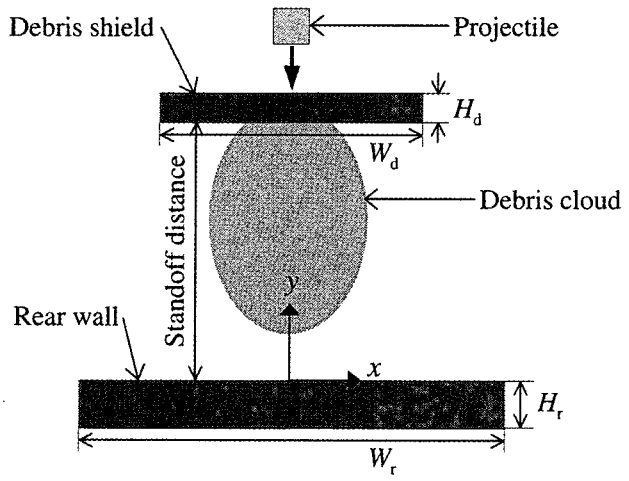

Figure 1 Schematic view of HVI of a projectile on a rear wall protected by a debris shield.

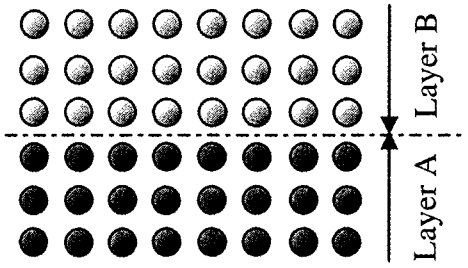

Figure 2 Schematic view of interface of laminated rear walls.

Table 2 Material properties of Gr/Ep lamina.

E_{11}(GPa)	E_{22}(GPa)	G_{12}(GPa)	G_{23}(GPa)	ν_{12}(−)	ν_{23}(−)
139	9.85	5.25	3.8	0.25	0.38
a_{66}(−)	Γ(−)	ρ_0 (g/cm^3)	C_0 (km/s)	ξ(−)	C_P (J/gK)
1.4	0.87	1.60	4.69	1.57	1.00

Tensile strength, fiber direction	1.45 (GPa)
Compressive strength, fiber direction	1.45 (GPa)
Tensile strength, transverse direction	0.260 (GPa)
Compressive strength, transverse direction	1.03 (GPa)
In-plane shear strength	0.465 (GPa)
Shear strength in the 2-3 plane	0.465 (GPa)

3.1.2 ***Rear walls*** : Figure 3 shows five types of the rear walls. Type 1 is the $[0/90]_s$ cross-ply Gr/Ep rear wall, and Types 2-A, B and 3-A, B are the hybrid composite rear walls which consist of a Gr/Ep laminate bonded with an aluminum plate. In Figure 3, the layer angle 0° means that the fiber orientation is parallel to the x axis, and the layer angle 90° means that the fiber orientation is perpendicular to the x-y plane. The rear walls are W_r=400 mm in width. The material properties of Gr/Ep lamina are given in Table 2.

Table 3 Impact velocities, projectile masses and debris shield thicknesses in numerical simulation.

	Impact velocities (km/s)	Projectile masses (g/cm)	Debris shield thicknesses (mm)
Case A	2.0 ~ 4.0	0.11	1.4
Case B	4.0	0.028 ~ 0.11	1.4
Case C	4.0	0.11	1.4 ~ 4.0

3.2 Numerical simulation results

Figure 4 illustrates the deformation and fracture behavior of the Gr/Ep rear wall of Type 1, whose thickness is H_r=16 mm. We find that the rear wall is perforated at the impact velocity 4 km/s, although not perforated at the impact velocity 3 km/s. Figure 5 shows the maximum of $\hat{E}$ ($=\int_0^\infty \hat{E}_t\,dt$) on the top surface of the rear wall, $\hat{E}_{max}$, for different impact velocities (Case A), projectile masses (Case B) and debris shield thickness (Case C) in Table 3,

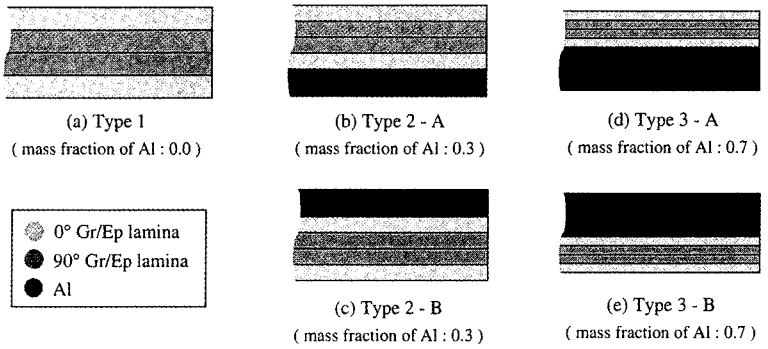

Figure 3 Laminate configurations of Gr/Ep and hybrid composite rear walls.

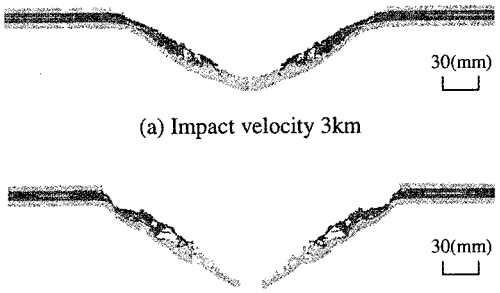

Figure 4 Deformation and fracture behavior of Gr/Ep rear wall.

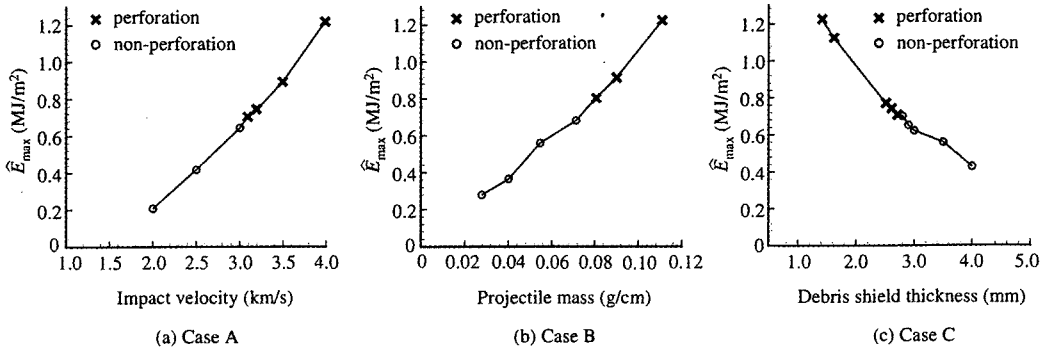

Figure 5 $\hat{E}_{max}$ versus impact velocity, projectile mass and debris shield thickness.

where $\hat{E}_t$ is the kinetic energy flux density of debris cloud on the top surface of the rear wall. In the figure, the cross symbols indicate perforation of the rear wall, and the open circle symbols non-perforation. We find that $\hat{E}_{max}$ obviously increases monotonically with increasing projectile velocity and projectile mass, and decreasing debris shield thickness. Figure 6 presents the smallest values of $\hat{E}_{max}$ in the perforation data and the largest values of $\hat{E}_{max}$ in the non-perforation data. It is found from the figure that the values of E_{max} at the ballistic limit, $\hat{E}_{max,b}$, are nearly identical at $\hat{E}_{max,b}=0.71\,MJ/m^2$, which independent of the impact velocity, the projectile mass and the debris shield thickness. From this result, it is suggested that $\hat{E}_{max,b}$ could be available to evaluate the ballistic limit of rear wall.

3.3 Ballistic limits of Gr/Ep and hybrid composite rear walls

Figure 7 shows $\hat{E}_{max,b}$ versus the thickness of Gr/Ep and hybrid composite rear walls. It is obvious from the figure that $\hat{E}_{max,b}$ increases with the rear wall thickness, and the hybrid composite rear walls exhibit better perforation resistance than the Gr/Ep rear wall. Moreover, the rear walls of Types 2-B and 3-B exhibit, respectively, better perforation resistance than the rear walls of Type 2-A and Type 3-A. From this result, we can state that it is effective to bond an aluminum plate on the top surface of Gr/Ep rear walls in order to improve the perforation resistance of the Gr/Ep rear walls.

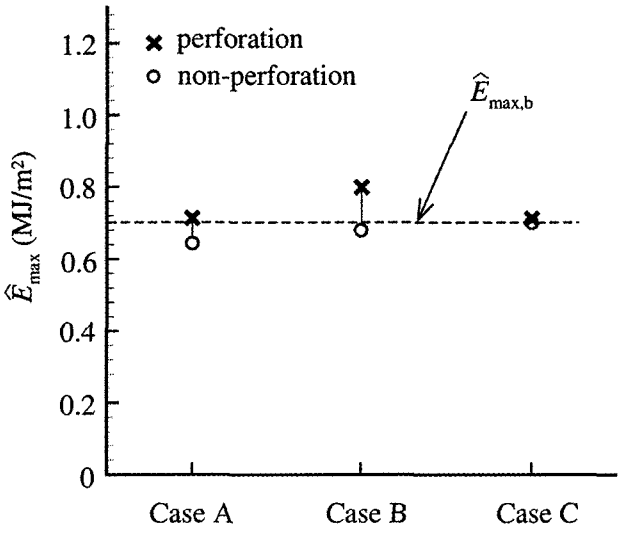

Figure 6 Ballistic limit of Gr/Ep rear wall.

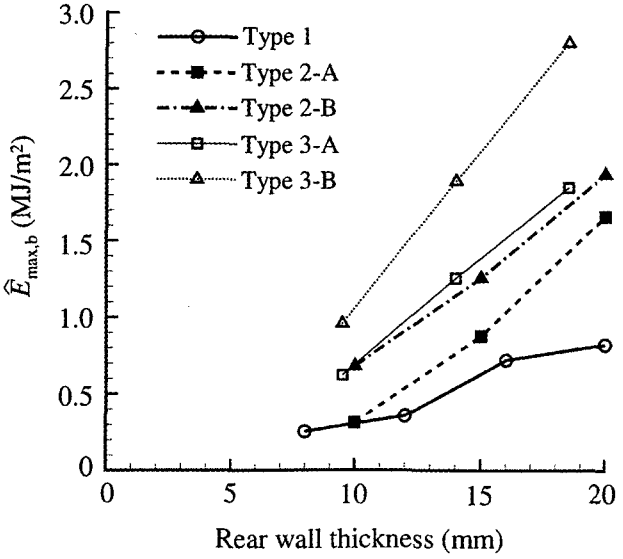

Figure 7 $\hat{E}_{max,b}$ versus thickness of Gr/Ep and hybrid composite rear walls.

4 Conclusions

We numerically simulated HVIs of a projectile on Gr/Ep and hybrid composite rear walls protected by a debris shield using the two-dimensional improved SPH method. Through the numerical simulation, we have evaluated the maximum value of the total kinetic energy of debris cloud through unit area on the top surface of rear wall, and suggested that $\hat{E}_{max,b}$ could be available to evaluate the ballistic limit of rear wall. Moreover, we have shown $\hat{E}_{max,b}$ versus the thickness of Gr/Ep and hybrid composite rear walls, and found that it is effective to bond an aluminum plate on the top surface of Gr/Ep rear walls in order to improve the perforation resistance of the Gr/Ep rear walls.

References

1. L. D. Libersky and A. G. Petschek, "Smoothed Particle Hydrodynamics with Strength of Materials," *Lect. Notes Phys.*, Vol. 395, pp. 248-257, (1991).
2. L. D. Libersky, A. G. Petschek, T. C. Carney, J. R. Hipp and F. A. Allahdadi, "High Strain Lagrangian Hydrodynamics," *J. Comput. Phys.*, Vol. 109, pp. 67-73, (1993).
3. C. J. Hayhurst, I. H. G. Livingstone, R. A. Clegg, R. Destefanis, and M. Faraud, "Ballistic Limit Evaluation of Advanced Shielding Using Numerical Simulations," *Int. J. Impact Eng.*, Vol. 26, pp. 309-320, (2001).
4. D. Palmieri, M. Faraud, R. Destefanis, and M. Marchetti, "Whipple Shield Ballistic Limit at Impact Velocities Higher than 7 km/s," *Int. J. Impact Eng.*, Vol. 26, pp. 579-590, (2000).
5. K. Shintate, H. Sekine, "Numerical Simulation of Hypervelocity Impacts of a Projectile on Laminated Composite Plate Targets by Means of Improved SPH Method," *Composite A*, Vol. 35, pp. 309-320, (2004).
6. J. L. Chen and C. T. Sun, "A Plastic Potential Function Suitable for Anisotropic Fiber Composites," *J. Compos. Mater.*, Vol. 27, pp. 1379-1390, (1993).
7. G. R. Johnson, and W. H. Cook, "Fracture Characteristics of Three Metals Subjected to Various Strains, Strain Rates, Temperatures and Pressures," *Eng. Fract. Mech.*, Vol. 21, pp. 31-48, (1985).
8. D. F. Medina, J. K. Chen, "Three-Dimensional Simulations of Impact Induced Damage in Composite Structures Using the Parallelized SPH Method," *Composites A*, Vol. 31, pp. 853-860, (2001).
9. J. A. Zukas, "*High Velocity Impact Dynamics*," Wiley, New York., pp. 186-280, (1990).